Engineering xxx (xxxx) xxx

Contents lists available at ScienceDirect

Engineering

journal homepage: www.elsevier.com/locate/eng

Research
Agricultural Engineering—Article

Stage-Specific Polymerization Mechanisms in Bio-Tar Unveiled by Single-Functional Model-Compounds: Dominant Roles of Unsaturated Oxygen Moieties

Yuxuan Sun [a], Lixin Zhao [a], Huiyan Zhang [b], Hui Zhou [c], Lili Huo [a], Jixiu Jia [a], Zonglu Yao [a,*]

[a] Key Laboratory of Low-carbon Green Agriculture in North China (Ministry of Agriculture and Rural Affairs), Institute of Environment and Sustainable Development in Agriculture, CAAS, Beijing 100081, China
[b] Key Laboratory of Energy Thermal Conversion and Control of Ministry of Education, School of Energy and Environment, Southeast University, Nanjing 210096, China
[c] Key Laboratory for Thermal Science and Power Engineering of Ministry of Education, Department of Energy and Power Engineering, Tsinghua University, Beijing 100084, China

ARTICLE INFO

Article history:
Received 13 October 2025
Revised 2 February 2026
Accepted 10 February 2026
Available online xxxx

Keywords:
Bio-tar
Bio-carbon
Polymerization
Model compound
Simulation

ABSTRACT

Bio-tar, a byproduct of biomass pyrolysis, poses environmental and processing challenges owing to its tendency to clog pipelines and its ecotoxicity. Converting bio-tar into functional carbon materials offers a sustainable route for waste valorization; however, the underlying thermal polymerization mechanisms remain poorly understood. Herein, we present a single-functional model-compound-assisted analytical strategy to elucidate reaction pathways and polymerization mechanisms in multifunctional group coupling systems. By constructing a model bio-tar (M-bio-tar) that reflects the chemical heterogeneity of real samples, we uncover a temperature-dependent, stage-specific polymerization mechanism comprising volatile release (≤ 200 °C), radical-driven crosslinking polymerization (200–400 °C), and carbon skeleton consolidation (≥ 300 °C). Radical dynamics involving alkyl and hydroxyl radicals ($R^{\bullet}$ and $HO^{\bullet}$) are key contributors to crosslinking processes, while oxygenated intermediates, such as aldehydes and furans, enhance polymerization efficiency via synergistic Diels–Alder and cyclization reactions. Structural evolution analyses reveal temperature-dependent trade-offs among graphitization, dehydrogenation, and porosity development. Temperature-mediated graphitization and heteroatom elimination result in biocarbons with tunable physicochemical properties. Thermodynamic calculations support the proposed oxygen-regulated reaction pathways and reveal the catalytic roles of unsaturated functionalities. These findings establish a mechanistic framework for engineering bio-tar-derived carbon materials that integrates biomass utilization and advanced material design, thereby advancing the rational development of sustainable carbon materials for energy and environmental applications within a circular bioeconomy.

1. Introduction

Pyrolysis is a pivotal technology for developing novel renewable energy systems, in which solid and gaseous products can serve as precursors for value-added materials or as direct energy sources [1,2]. However, the widespread adoption of pyrolysis technology faces a critical bottleneck: the persistent formation of bio-tar, viscous byproducts generated by the condensation of pyrolytic gaseous products, typically accounting for 10%–20% of the total output [3–5]. Characterized by a dew point below 100 °C, bio-tar readily condenses in downstream pipelines and equipment, leading to frequent operational disruptions due to persistent clogging. More critically, its chemical composition, dominated by volatile aromatic compounds, exhibits high environmental persistence and marked ecological toxicity [6–8]. Existing mitigation strategies cannot effectively address the engineering challenges of system maintenance and the environmental risks associated with unintended emissions. For condensed liquid bio-tar, the prevailing strategy relies on treating it as an energy precursor or chemical feedstock to increase its utility and enable efficient processing [9]. Although its high carbon content (60–70 wt%) and low ash composition (< 1 wt%) position bio-tar as a potential energy carrier, incomplete combustion and operational challenges stemming from its high viscosity hinder its practical implementation [10].

* Corresponding author.
E-mail address: yaozonglu@caas.cn (Z. Yao).

https://doi.org/10.1016/j.eng.2026.02.034

Please cite this article as: Y. Sun, L. Zhao, H. Zhang et al., Stage-Specific Polymerization Mechanisms in Bio-Tar Unveiled by Single-Functional Model-Compounds: Dominant Roles of Unsaturated Oxygen Moieties, Engineering, https://doi.org/10.1016/j.eng.2026.02.034

Unfortunately, alternative methods such as distillation or solvent extraction face limitations because of the complex intercomponent crosslinking and overlapping physicochemical characteristics of the material.

Research efforts directed to overcome such barriers have led to the development of a thermal polymerization strategy that directly converts bio-tar into solid bio-carbon materials [11,12], simultaneously addressing the production of novel carbon materials and bio-tar treatment challenges [13]. Owing to its higher graphitization and lower ash content, bio-carbon has great potential for high-performance applications, such as energy storage electrodes and adsorbents. However, two major challenges remain: enhancing production yield and achieving precise control over the physicochemical properties of the resulting materials [14]. During thermal polymerization, light volatile fractions are prone to evaporation or cracking, substantially reducing bio-carbon yield. In addition, the compositional heterogeneity of bio-tar results in diverse polymerization behaviors, among which only the crosslinking mechanisms among its complex constituents are partially understood. Aliphatic hydrocarbons and low-ring aromatic compounds are known to undergo secondary reactions such as addition and condensation under thermal conditions to form polycyclic aromatic hydrocarbons (PAHs), which ultimately polymerize into bio-carbons. Further investigations have advanced rapid polymerization processes and introduced oxygenated organic compounds as regulatory means to produce structurally stable bio-carbon [15–17]. However, process parameters, such as heating rate and temperature profile, offer limited control over reaction pathways toward desired properties, thereby restricting the optimization of material performance in downstream applications [18]. Overcoming these limitations requires a deeper understanding of the transformation pathways specific to individual components and the mechanisms governing bio-carbon formation under thermal conditions.

Unlike conventional biomass feedstocks, bio-tar, which are sophisticated organic mixtures, pose significant challenges for complex reaction systems investigation because of their resistance to simple component categorization [19–21]. Notably, the constituent compounds of bio-tar display significant variability in atomic composition, molecular size, and bonding configurations, all of which critically affect the interpretation of polymerization mechanisms [22]. Considering that polymerization inherently involves bond cleavage and reformation among specific functional groups, we have innovatively used a classification framework that prioritizes functional group characteristics to analyze bio-tar. Although lower-priority functional groups may persist as substituents, using model compounds with single dominant functional groups significantly simplifies the elucidation of multifunctional-group-mediated polymerization pathways. This approach directly addresses bio-tar heterogeneity by decoupling multifunctional-group-mediated interactions, enabling more accurate mechanistic insights into the complex transformation behavior of bio-tar.

In this study, we propose a single-function model-compound-assisted strategy to investigate bio-tar polymerization by constructing a model bio-tar (M-bio-tar) using model organic compounds that reflect compositional heterogeneity. By integrating experiments and density functional theory (DFT) simulations, we systematically analyzed the polymerization mechanisms and identified critical crosslinking pathways governed by key functional groups. Our results reveal the catalytic role of unsaturated oxygen-containing moieties (particularly aldehyde groups and furan rings) in promoting polymerization efficiency and directing the formation of bio-carbon frameworks through synergistic reactions. We further elucidate the hierarchical assembly mechanism of bio-carbon skeletons within complex reaction networks and propose a temperature-mediated, stage-specific bio-tar polymerization mechanism that follows distinct reaction pathways at different temperatures. By revealing the molecular-level mechanisms governing thermal conversion in mixed organic systems, this work establishes a fundamental understanding of bio-carbon synthesis. These findings provide critical theoretical and technical foundations for sustainable bio-tar valorization and the development of novel biobased carbon materials, advancing the field toward the efficient utilization of biomass resources in energy and materials science.

2. Materials and methods

2.1. Chemicals

The bio-tar utilized in this study was produced via slow pyrolysis of corn stalks collected from Hebei Province, China, under controlled conditions at 600 °C for 40 min, followed by condensation at 100 °C. Detailed characterization data for the bio-tar are provided in Table S1 in Appendix A. Anhydrous ethanol, benzyl alcohol, benzoic acid, benzaldehyde, methyl benzoate, phenol, furan, 4-hydroxy-4-methyl-2-pentanone, glucose, paraffin, and toluene—were sourced from Shanghai Macklin Biochemical Technology Co., Ltd. High-purity nitrogen for experimental operations and analytical measurements was supplied by Beijing Yongsheng Gas Technology Co., Ltd (China).

2.2. Bio-tar composition profiling and M-bio-tar preparation

Bio-tar composition profiling was performed via gas chromatography–mass spectrometry (GC–MS, 7890B-5977A; Agilent, USA) in triplicate, and the average relative content of the components was reported as the bio-tar composition profile (Table S2 in Appendix A). A 1 μL aliquot of concentrated bio-tar sample (prepared by dilution in acetone to 1 wt%) was injected in splitless mode onto a DB-5 capillary column (30 m × 0.25 mm × 0.25 μm) using high-purity helium as the carrier gas at 1.78 $mL{\cdot}min^{-1}$. The injector, interface, and ion source temperatures were maintained at 250, 280, and 230 °C, respectively, with a split ratio of 20:1. The oven temperature program was initiated at 40 °C (2 min hold), followed by ramping to 200 °C at 8 $°C{\cdot}min^{-1}$ (3 min hold) and then to 280 °C at 4 $°C{\cdot}min^{-1}$ (6 min hold) [23]. An electron ionization (EI) source at 70 eV was employed for fragmentation, with mass spectra acquired across a mass-to-charge ratio (m/z) range of 50–550.

The M-bio-tar was carefully engineered according to the compositional profile of bio-tar, derived from the normalized peak area data obtained via mass spectrometry. It includes representative model compounds selected to reflect major functional group categories: benzyl alcohol (alcohols), benzoic acid (carboxylic acids), benzaldehyde (aldehydes), phenol (phenolic compounds), methyl benzoate (esters), furan (furans), 4-hydroxy-4-methyl-2-pentanone (ketones), glucose (carbohydrates), paraffin (aliphatic hydrocarbons), and toluene (aromatic hydrocarbons). The corresponding ratios for each compound are provided in Table S3 in Appendix A. The mixture was prepared by dissolving all components in a water bath at 60 °C under stirring until a homogeneous oil-phase mixture was achieved, as illustrated in Fig. S1 in Appendix A.

2.3. Thermal polymerization characterization

Thermogravimetry–differential thermogravimetry analysis (TG–DTG, STA8122 analyzer; Rigaku, Japan) was conducted on both bio-tar and M-bio-tar under N_2 atmosphere, with a heating rate of 10 $°C{\cdot}min^{-1}$ from 50 to 800 °C. For evolved gas analysis during thermal polymerization, pyrolytic gas chromatography–mass spectrometry (Py-GC–MS, Frontier PY3030D pyrolyzer coupled

with Thermo ISQ™ LT TRACE™ 1310 GC–MS, Japan/USA) was conducted under identical chromatographic parameters as described for compositional profiling (see Methods section "bio-tar composition profiling"). The functional group evolution of the gaseous products was monitored via thermogravimetry–infrared spectroscopy (TG–IR, NETZSCH TG 209 F3 Libra® combined with Bruker TENSOR27 FTIR, Germany) from 4000 to 400 cm^{-1}. Simultaneously, temperature-dependent gas-phase ion profiles were analyzed via thermogravimetry–mass spectrometry (TG–MS, MS SPECTROMETER LC-D200M PRO, Japan) with a *m/z* detection range of 2–200. All three evolved gas analyses (Py-GC–MS, TG–IR, and TG–MS) were systematically performed under a N_2 atmosphere with a heating rate of 10 °C·min^{-1} to target temperatures of 300, 400, and 500 °C, respectively, and held for 30 min upon reaching each target temperature to correlate the thermal degradation pathways with the polymerization stages.

The distribution of carbon- and oxygen-centered radicals during bio-tar thermal polymerization was assessed using electron paramagnetic resonance (EPR, EMXplus 300 A; Bruker, Germany). Experiments were performed at five selected temperatures (100, 200, 300, 400, and 500 °C), with a consistent heating rate of 10 °C·min^{-1}. Radical concentrations were measured immediately upon reaching each temperature point. To ensure the precise and sensitive detection of transient radicals generated throughout the successive stages of polymerization, EPR spectra were collected under finely tuned conditions: a modulation frequency of 100 kHz, a microwave frequency of 9.85 GHz, receiver gain of 1000 dB, a central magnetic field of 3510 G (1 G = 10^{-5} T), and a scan width of 100 G.

2.4. DFT calculations

Polymerization pathways with model compounds were examined by performing DFT calculations using Gaussian 16. Geometric optimizations and single-point Gibbs free energy calculations were conducted at the B3LYP-D3BJ/6-311G(d,p) level to assess the thermodynamic feasibility of the reactions. Molecular orbital analyses, including the distributions of the highest occupied molecular orbital (HOMO) and lowest unoccupied molecular orbital (LUMO) for each model compound, were performed using Multiwfn 3.8 (dev) with the 6-31G basis set. Vibrational frequency calculations confirmed the absence of imaginary frequencies at optimized geometries, ensuring true energy minima. The reaction selectivity of the M-bio-tar system was simulated using frontier molecular orbital energy gaps and charge transfer parameters. Structural visualizations and orbital energy diagrams were generated using VMD 1.9.3, with data extracted from Gaussian checkpoint files [24].

2.5. Preparation and characterization of polymerization products

Polymerized products were synthesized in a tubular furnace using 30 g of either bio-tar or M-bio-tar as feedstocks through a controlled process under a N_2 atmosphere flowing at 200 mL·min^{-1}. The polymerization was conducted at target temperatures of 300, 400, and 500 °C with a 2 h holding time and a heating rate of 10 °C·min^{-1}. Postreaction, the samples were sequentially rinsed with anhydrous ethanol and deionized water. The purified products were subsequently dried at 105 °C for 12 h. All the samples derived from the bio-tar and M-bio-tar were systematically designated BC-*x* and MBC-*x*, respectively, where *x* corresponds to the polymerization temperature.

Elemental composition was assessed using an Elementar Vario EL cube analyzer (Germany). Surface chemical functionalities, specifically C1s and O1s spectra, were analyzed using X-ray photoelectron spectroscopy (XPS, ESCALAB 250 Xi; Thermo Fisher, USA). Functional group distributions and bonding characteristics were examined using Fourier-transform infrared spectroscopy (FTIR, Nicolet iS5; Thermo Fisher) across a spectral range of 4000–400 cm^{-1}. Textural properties, including pore structure and specific surface area, were characterized via nitrogen adsorption at 77 K using a Micromeritics ASAP 2020 instrument (USA). All samples were degassed under vacuum at 300 °C for 6 h before analysis. The Brunauer–Emmett–Teller (BET) surface area (S_{BET}) was determined using adsorption data in the relative pressure (P/P_0) range of 0.04–0.20, and the total pore volume (V_{total}) was calculated from N_2 adsorption at P/P_0 = 0.99. The micropore volume (V_{micro}) and pore size distribution (PSD) were modeled using a two-dimensional non-local density functional theory (2D-NLDFT) approach. Crystallinity was assessed via X-ray diffraction (XRD, Rigaku Ultima IV, Japan), and the degree of graphitization was evaluated via laser confocal Raman spectroscopy (DXR 2xi; Thermo Fisher). Morphological features were examined using scanning electron microscopy (SEM, Apreo 2S; Thermo Fisher).

3. Results and discussion

3.1. Thermal polymerization dynamics and mass loss behavior

The thermal conversion of bio-tar into functional carbon materials via polymerization is inherently limited by competitive evaporation and cracking processes, which reduce bio-carbon yields. To elucidate the underlying mechanisms, the thermal polymerization behaviors of bio-tar and a rationally designed M-bio-tar were systematically compared via TG analysis coupled with compositional and elemental characterization. GC–MS profiling (Fig. 1(a)) indicated that bio-tar is a heterogeneous mixture primarily composed of phenols (31.8%), sugars (16.7%), ketones (11.1%), and esters (10.4%), with smaller proportions of alcohols, aldehydes, acids, furans, and hydrocarbons (Fig. 1(b)). This compositional complexity renders mechanistic investigations challenging owing to the occurrence of overlapping decomposition pathways. To overcome this, M-bio-tar was synthesized using ten representative compounds (benzyl alcohol, benzoic acid, 4-hydroxy-4-methyl-2-pentanone, phenol, methyl benzoate, furan, benzaldehyde, glucose, toluene, and paraffin), which were selected to represent the major chemical classes identified in bio-tar (Note S1 in Appendix A). This model system facilitates mechanistic analysis by isolating polymerization pathways associated with specific functional groups. Importantly, its thermal polymerization behavior, including mass loss and polymerization yield, is primarily dictated by small-molecule model compounds, leading to characteristics that differ from those observed in real bio-tar systems. This divergence stems, from the simplified nature of the model compounds relative to the macromolecular complexity of bio-tar and does not fundamentally hinder the exploration of the underlying reaction mechanisms [25,26]. Instead, the reduction in structural complexity enables a more precise identification of elementary reaction steps while preserving fidelity to the core chemical principles governing crosslinking polymerization [27–29].

Under a nitrogen atmosphere, the TG–DTG curves of the bio-tar and M-bio-tar (Fig. 1(c)) exhibited distinct mass loss stages. In the initial heating phase (50–150 °C), the bio-tar showed gradual mass loss due to the evaporation of small volatile molecules (e.g., aldehydes and alcohols), whereas the dominance of low-molecular-weight volatiles in M-bio-tar resulted in an accelerated mass loss. As the temperature increased to 150–250 °C, the bio-tar underwent concurrent evaporation, cracking, and incipient thermal polymerization of macromolecular phenols and sugars, reaching a peak mass loss rate of 0.40%·°C^{-1} at 263.17 °C. In contrast, M-bio-tar displayed a decline in mass loss rates during this phase, which can be attributed to the occurrence of aromatization and condensation among components. At temperatures exceeding 260 °C, both

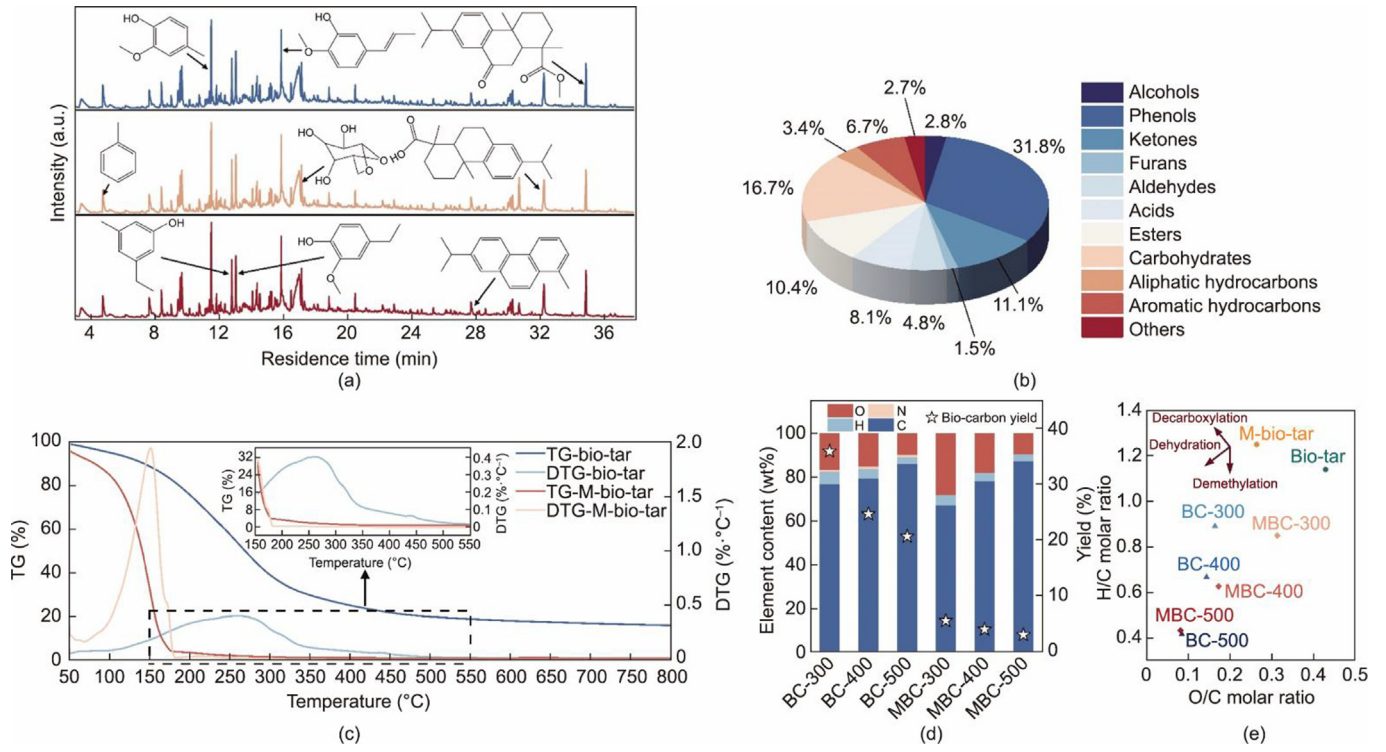

Fig. 1. Physicochemical and thermal polymerization characteristics of bio-tar. (a) Representative triplicate GC–MS profiles of bio-tar. (b) Compositional characteristics of bio-tar components (normalization results of peak area in MS). (c) Comparative TG–DTG curves of bio-tar and M-bio-tar. (d) Elemental distribution and production yield of BC-x and MBC-x. (e) Atomic molar ratios (O/C and H/C) of bio-tar, M-bio-tar, and bio-carbons. BC-300, BC-400, and BC-500 denote the bio-carbons derived from bio-tar polymerized at 300, 400, and 500 °C, respectively. Similarly, MBC-300, MBC-400, and MBC-500 represent the bio-carbons derived from model bio-tar under the same respective polymerization temperatures.

systems exhibited intensified polymerization and carbonization processes, reflected in a slower rate of mass loss due to ongoing crosslinking reactions and the breakdown of thermally resilient intermediates [30–32].

Notably, M-bio-tar underwent more pronounced evaporation and cracking at lower temperatures, resulting in lower bio-carbon yields compared with bio-tar, because the inhibition of cracking evaporation by the complex matrix was absent in the model system. Both feedstocks showed decreasing bio-carbon yields with increasing pyrolysis temperatures (Fig. 1(d)), which aligns with the TGA results; specifically, higher temperatures promoted polymerization but concurrently intensified cracking-induced solid loss. Elemental molar ratio analysis (Fig. 1(e) and Table S4 in Appendix A) revealed the progressive depletion of hydrogen and oxygen in bio-carbon with increasing temperature, indicating sustained dehydration and decarboxylation alongside increased graphitization, a trend consistent with conventional biomass pyrolysis. These findings underscore the temperature-dependent trade-off between polymerization efficiency and thermal degradation.

Our results demonstrate that bio-tar polymerization is governed by the interplay of competitive investigation, component-specific decomposition, and cross-reaction-driven carbonization. Crucially, M-bio-tar successfully simulated key thermal behaviors and product characteristics of bio-tar, providing a simplified platform for mechanistic exploration. In the next sections, these thermokinetic profiles will be correlated with free radical dynamics (via EPR), gaseous product evolution (via TG–MS and TG–IR), and carbon skeleton structural features to fully elucidate the polymerization–carbonization mechanisms.

3.2. Volatile evolution and reaction pathways

The volatile species distribution profiles of bio-tar and M-bio-tar (Figs. 2(a) and (b) and Figs. S2 and S3 in Appendix A) revealed pronounced temperature-dependent trends. Phenolic compounds dominate bio-tar volatiles because of their high initial abundance and thermal volatility. In contrast, the phenolic fraction in M-bio-tar volatiles decreased with increasing polymerization temperatures, dropping to 6.03% at higher thermal conditions, even though both feedstocks followed similar temperature-dependent patterns. This decline is primarily due to the increased liberation of hydrocarbons—particularly those originating from paraffinic structures—at elevated temperatures. Higher temperatures facilitate the deoxygenation of oxygen-rich intermediates, such as esters and acids, yielding hydrocarbon precursors such as benzene and biphenyl that readily transform into carbonaceous structures. This trend reflects the intensified breakdown of oxygenated compounds and their subsequent aromatization, confirming the occurrence of condensation during bio-tar polymerization.

The relative abundance of model volatile compounds (Fig. 2(c)) provides further evidence for functional group-specific behaviors. At a polymerization temperature of 300 °C, volatile substances are predominantly model compounds, and the higher biochar yield observed under these conditions suggests that lower temperatures favor the formation of carbon precursors and skeletal frameworks while effectively suppressing the release of volatiles caused by secondary cracking post-polymerization. Interestingly, saccharide components such as glucose, undergo effective carbonization and polymerization at relatively low temperatures, a behavior intrinsically related to their pyrolysis characteristics. The

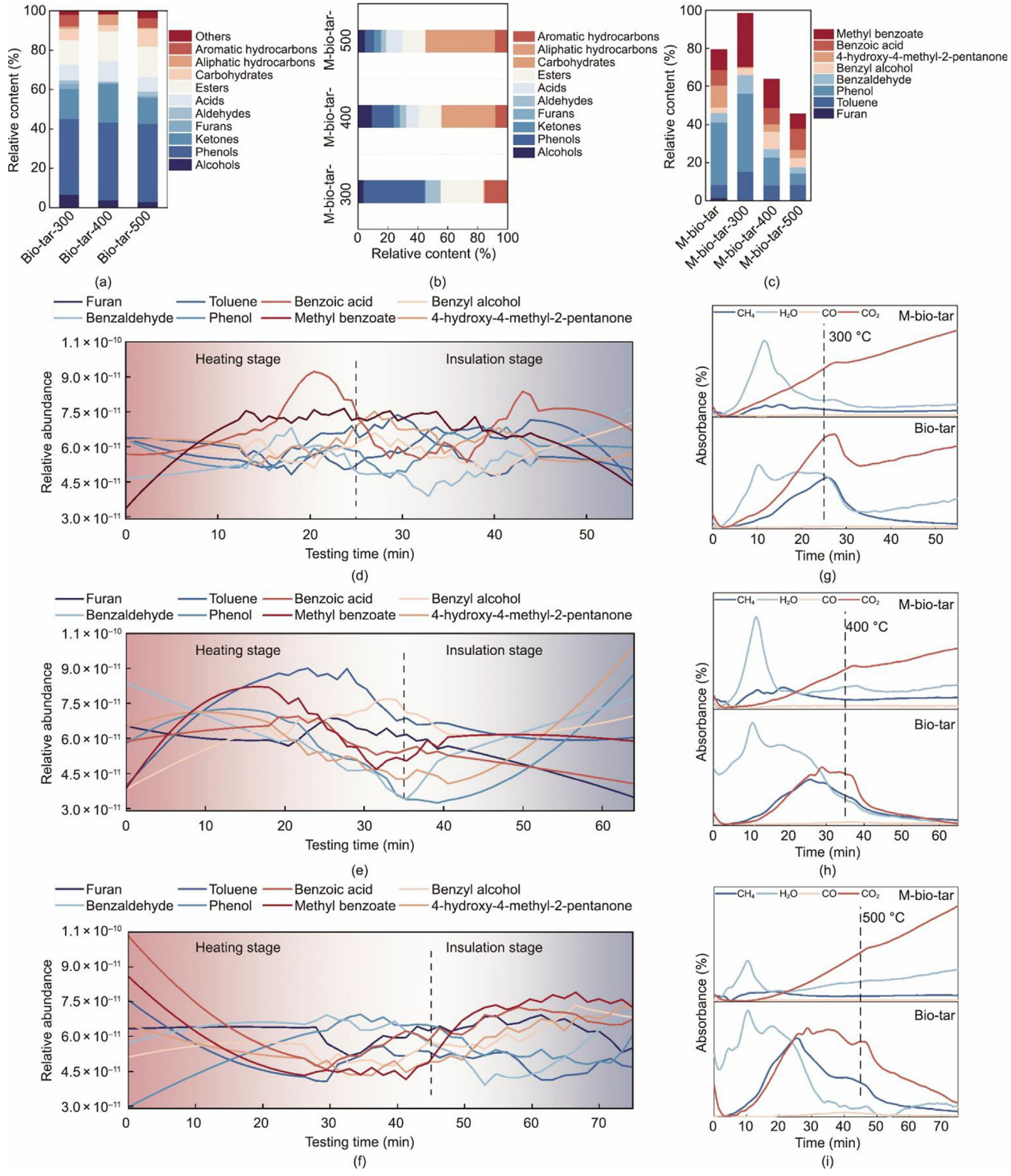

Fig. 2. Thermal volatilization characteristics of bio-tar. (a) Compositional profile of volatile components from bio-tar thermal polymerization (normalization results of peak area in MS). (b) Compositional profile of volatile components from M-bio-tar thermal polymerization. (c) Volatilization mechanisms of major components in M-bio-tar. TG–MS profiles of major components in M-bio-tar under programmed heating to (d) 300, (e) 400, and (f) 500 °C at 10 °C·min^{-1} followed by 30 min isothermal holding. Comparative TG–IR profiles of small-molecule volatile gases (CH_4, H_2O, CO, and CO_2) from bio-tar and M-bio-tar under programmed heating to (g) 300, (h) 400, and (i) 500 °C at 10 °C·min^{-1} followed by 30 min isothermal holding. bio-tar-300, bio-tar-400, and bio-tar-500 denote the controlled pyrolysis processes of bio-tar at 300, 400, and 500 °C, respectively. Similarly, M-bio-tar-300, M-bio-tar-400, and M-bio-tar-500 represent the controlled pyrolysis processes of model bio-tar under the same respective temperatures.

calculated bio-carbon conversion efficiency of 32.96% from glucose exceeds previously reported biochar yields from glucose pyrolysis. This result indicates that saccharides are the primary but not the sole contributors to the polymerization–carbonization process [33,34], acting as primary precursors in the formation of aromatic networks in concert with secondary constituents during thermal transformation.

In contrast, polymerization at 500 °C yields negligible carbohydrate-derived volatiles (0.21%) in the model systems, whereas bio-tar polymerization results in a marked increase in carbohydrate volatiles from 5.86% at 300 °C to 9.13% at 500 °C. This suggests that carbohydrate constituents primarily undergo polymerization and become immobilized within the solid matrix at temperatures below 300 °C. Subsequent increases in temperature induce secondary cracking of these solid-phase products, facilitating deoxygenation and promoting the graphitization of the resulting bio-carbon. Furan, which has an epoxy structure, displayed suppressed volatility and decreased abundance with increasing temperature, indicating its dual role as a carbonization intermediate (via sugar decomposition) and a participant in Diels–Alder reactions [35–38]. The volatility of aldehydes mirrors that of phenolic compounds because of their propensity for dehydration to form alkenyl-rich carbon precursors, whereas ketones remain relatively inert owing to their stable carbonyl groups.

To further investigate bio-carbon formation, thermogravimetric analysis conducted under controlled heating rates (Figs. S4–S6 in Appendix A) was integrated with in situ TG–MS (Figs. 2(d)–(f) and Figs. S7–S12 in Appendix A) and TG–IR (Figs. 2(g)–(i) and Figs. S13–S18 in Appendix A) to monitor volatile species. The decrease in the signals of furan (m/z = 68) and benzaldehyde (m/z = 106) during the heating and isothermal stages indicates their active participation in polymerization reactions. Toluene (m/z = 92) remained stable throughout the isothermal phases, reflecting the stabilization and incorporation of aromatic precursors. Notably, a resurgence of oxygenated volatiles, such as benzyl alcohol, phenol, and 4-hydroxy-4-methyl-2-pentanone, was observed at 400 °C (Fig. 2(e)), suggesting that this temperature is optimal for oxygen elimination and polymerization efficiency. TG–IR analysis highlighted temperature-dependent decarbonylation (CO_2 at 2380 cm^{-1}) and dehydrogenation (H_2O at 3566 cm^{-1}), driven by carboxylic acid decarboxylation and aldehyde dehydration. Weak CO signals (2100 cm^{-1}) indicated limited carbonyl cleavage, whereas strong CH_4 signals (3015 cm^{-1}) at higher temperatures implied methyl group cyclization from esters (e.g., methyl benzoate) and aliphatic chains [39–42].

Collectively, these results support a three-stage bio-tar polymerization pathway:

(1) Volatile evaporation (≤ 200 °C): Light oxygenates (alcohols, ketones, and phenols) evaporate, accompanied by ester cracking, acid decarboxylation, and sugar/aldehyde dehydration, releasing CO_2 and CH_4.

(2) Intermediate cracking and polymerization (200–400 °C): Oxygenated intermediates decompose into reactive fragments (e.g., phenolic radicals and furanic species) and recombine via Diels–Alder or etherification reactions to form carbon precursors. Aliphatic chain cyclization releases CH_4.

(3) Carbonization (≥300 °C): Aromatic and alicyclic precursors undergo dehydrogenation and graphitization, with residual oxygen eliminated as small molecules.

In contrast with the complex and reactive nature of bio-tar, which promotes rapid cross-reactions, the simplified molecular structure of M-bio-tar enabled a more precise identification of individual functional group contributions. This mechanistic insight provides a foundation for the strategic development of bio-tar-derived carbon materials by disentangling and analyzing intricate reaction pathways.

3.3. Free radical-driven crosslinking mechanism

EPR and XPS were employed to systematically investigate the critical role of radicals in mediating crosslinking and functional group transformations during the thermal polymerization of bio-tar and M-bio-tar. The EPR spectra of bio-tar (Fig. 3(a)) and M-bio-tar (Fig. 3(b)) at various polymerization temperatures exhibited similar resonance signals in the 3320–3420 G range, with the signal intensities increasing proportionally to temperature [43]. This confirms temperature-dependent radical generation and the concurrent occurrence of cracking reactions, which reduce bio-carbon yields at elevated temperatures. Spectral deconvolution (Figs. S19 and S20 in Appendix A) revealed the presence of three primary radical species: hydrogen radicals ($H^•$), alkyl radicals ($R^•$), and hydroxyl radicals ($HO^•$). The relative abundance trends (Fig. 3(c)) indicated a dynamic shift in radical populations during polymerization [44]. Peak deconvolution of the XPS spectra of BC-x and MBC-x allowed identifying four distinct carbon-based functional groups through peak deconvolution (Figs. 3(d)–(g), Figs. S21 and S22 and Table S5 in Appendix A): sp^2 carbon (sp^2-C, 284.4 eV), sp^3 carbon (sp^3-C, 284.9 eV), C–O bonds from ethers or alcohols (285.5 eV), and carboxyl groups (O–C=O, 288.8 eV). Correspondingly, four oxygen-based species were observed: carbonyl groups (C=O, 532.6 eV), ether/alcohol C–O (531.1 eV), carboxyl groups (533.1 eV), and hydrophilic –OC moieties (535.8 eV) [45–47].

In bio-tar, $R^•$ and $HO^•$ dominated throughout the heating process, with consistent radical distributions across temperatures. In contrast, M-bio-tar presented a greater relative $HO^•$ abundance (29.9% average increase compared with bio-tar), which was attributed to phenol-dominated radical generation in the simplified system. Hydrocarbon components (e.g., toluene and paraffin) primarily produce $R^•$ and a lower amount of $H^•$. Elevated temperatures increase $R^•$ contributions due to ester decomposition (e.g., methyl benzoate), whereas decreased $H^•$ and $HO^•$ abundances correlate with aldehyde polymerization into olefinic structures and sugar-derived furanic intermediates. The concurrent reduction in sp^2-C content (Fig. 3(d)) further supports the gradual conversion of unsaturated groups (e.g., alkenes, aldehydes, and phenyls) into graphitic carbon frameworks. A sharp decrease in aromatic carbonyl groups at higher temperatures indicates loss of phenyl structures, facilitating carbonization. Notably, the carboxyl group abundance increased with temperature, driven by decarboxylation and radical-mediated oxygen elimination, which is consistent with the EPR-detected $H^•$ dynamics [48,49].

The functional group distributions in BC-300 and MBC-300 differed because of the higher initial oxygen content and small-molecule composition of M-bio-tar, which favored C–O retention. Unlike MBC, BC contains fewer oxygen functionalities (except carboxyl groups), highlighting fewer crosslinking pathways in the model system and enhanced oxygen removal via radical recombination in the heterogeneous matrix of biochar.

These results corroborate the bio-tar polymerization pathway inferred from volatile profiling. At lower temperatures (≤ 200 °C), the cleavage of unstable bonds initiates radical formation, driving the fragmentation and volatilization of light oxygenates and emitted, small gaseous molecules. Within the intermediate temperature range of 200–400 °C, radicals originating from phenolic and carbohydrate constituents produce unsaturated oxygenated intermediates, such as aldehydes and furans, which subsequently undergo Diels–Alder condensation and cyclization, forming key carbonaceous precursors. At higher temperatures (≥ 300 °C), persistent radical activity promotes further dehydrogenation and the progression toward graphitized, oxygen-depleted bio-carbon. This integrated view of radical dynamics and functional group transformations enhances the mechanistic comprehension of bio-tar

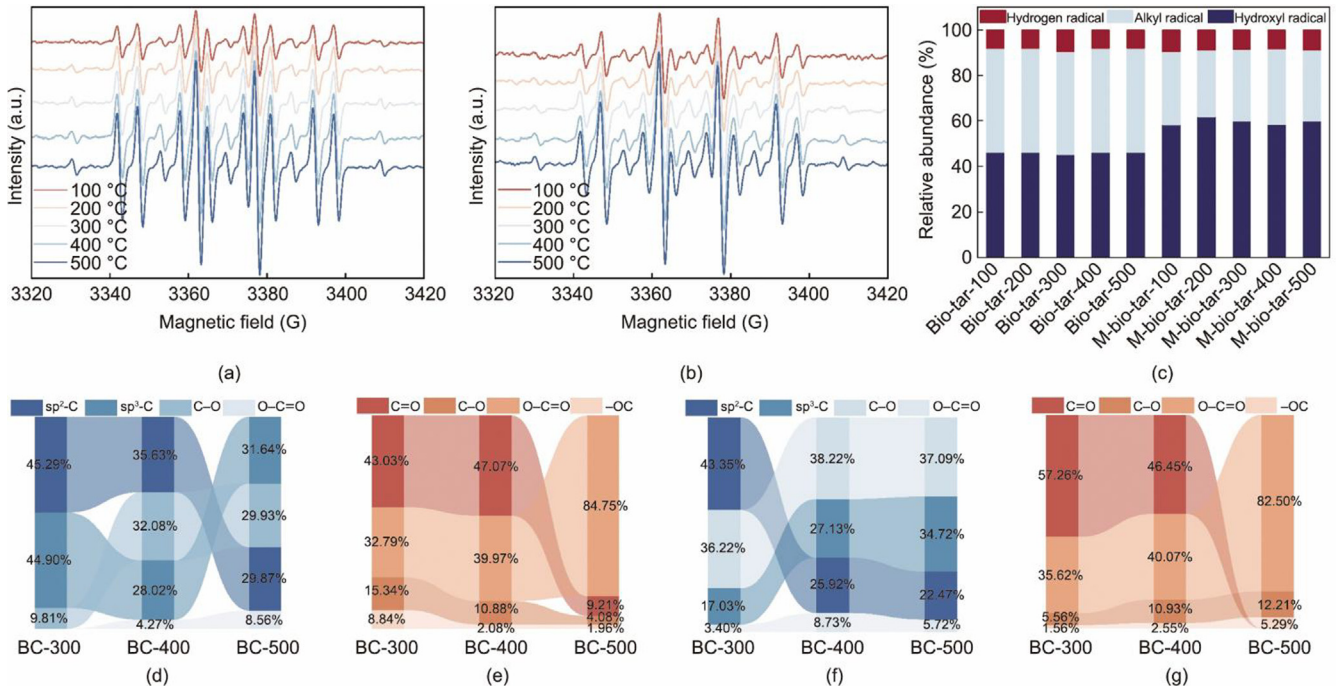

Fig. 3. Free radical distribution in the polymerization products and functional group characteristics in the polymerization products. (a) EPR spectra of bio-tar at varying polymerization temperatures. (b) EPR spectra of M-bio-tar at varying polymerization temperatures. (c) Relative abundance of free radicals during polymerization. Distribution of functional groups in the bio-tar polymerization products: (d) carbon-containing groups, (e) oxygen-containing groups. Distribution of functional groups in the M-bio-tar polymerization products: (f) carbon-containing groups, (g) oxygen-containing groups. bio-tar-300, bio-tar-400, and bio-tar-500 denote the controlled pyrolysis processes of bio-tar at 300, 400, and 500 °C, respectively. Similarly, M-bio-tar-300, M-bio-tar-400, and M-bio-tar-500 represent the controlled pyrolysis processes of model bio-tar under the same respective temperatures.

carbonization and provides strategic guidance for optimizing crosslinking processes in carbon material engineering.

3.4. Structural evolution of the bio-carbon matrix

The structural evolution of BC-*x* and MBC-*x* during thermal polymerization was systematically characterized via spectroscopic, morphological, and crystallographic analyses. Raman spectroscopy results reveal that all samples exhibit two distinct characteristic peaks at approximately 1350 and 1580 cm^{-1}, corresponding to the typical D-band (defect-induced band) and G-band (graphitic carbon vibration band) of carbon materials, respectively. As depicted in Fig. 4(a), the intensity ratios of D-band and G-band (I_D/I_G) (BC-*x*: 0.93–0.82; MBC-*x*: 0.89–0.62) and H/C molar ratios (BC-*x*: 0.89–0.41; MBC-*x*: 0.85–0.43) consistently decreased with increasing temperature, reflecting a progression toward greater graphitic structure and extensive dehydrogenation. This inverse trend underscores the pivotal role of hydrogen loss in the development of a consolidated carbon skeleton, in alignment with mechanisms driven by radical-induced crosslinking. FTIR spectra (Fig. 4(b)) were used to evaluate the functional group dynamics. The spectra of BC-300 and MBC-300 exhibited prominent –OH (3420 cm^{-1}), aliphatic C–H (2900 cm^{-1}), and C=O (1700 cm^{-1}) bands [50–52]. Meanwhile, the reduced –OH intensity in the spectra of BC-500 and MBC-500 confirmed dehydration-driven condensation, whereas the sharp attenuation of C=O aligned with the XPS results and the decarbonylation detected via TG–IR. The residual C–O peak (1030 cm^{-1}) in the spectrum of BC-500 suggested that ether crosslinking was facilitated by the native esters of bio-tar. The persistent aromatic C=C (1610 cm^{-1}) bands across all temperatures confirmed the occurrence of progressive aromatization [53,54].

The temperature hysteresis between carbon skeleton formation and volatile release, exacerbated by the compositional complexity of bio-carbon, was evident in the SEM images (Fig. 4(c)) and pore structure analyses. BC-*x* and MBC-*x* exhibited glassy fracture surfaces typical of amorphous carbons, with negligible porosity, which is consistent with the BET surface area measurements (Fig. 4(d), Table S6 in Appendix A). Both systems displayed low surface areas (< 1.5 $m^2 \cdot g^{-1}$), with BC-500 showing no detectable nitrogen adsorption due to pore collapse. The low micropore volume fractions (< 16%) further supported delayed pore evolution relative to volatile release. MBC-*x* exhibited marginally greater surface areas, attributable to the reduced temperature hysteresis in the simplified model system. The XRD patterns (Figs. 4(e) and (f)) revealed crystallographic evolution: the (002) diffraction peaks of BC-300 and MBC-300 shifted to lower diffraction angle (2θ) values (23°), reflecting greater interlayer spacing at lower temperatures [55]. As the degree of polymerization increased with temperature, the interlayer spacing decreased, consistent with the SEM observations.

Collectively, these findings indicate that moderate polymerization temperatures are optimal for balancing porosity, graphitic order, and yield. The multicomponent synergy of bio-tar enhanced crosslinking efficiency but introduced structural heterogeneity. The interplay of dehydrogenation, functional group elimination, and pore dynamics underscores thermal polymerization as a versatile route to tailor the functional architecture of bio-carbons. These insights advance the rational design of bio-tar-derived carbons for applications requiring tunable structural and surface properties. Future studies should focus on guiding the formation of more developed pore structures during polymerization by optimizing precursor composition or introducing templating agents. Furthermore, post-synthesis treatments, such as activation or heteroatom doping, are promising strategies for enhancing specific surface area and surface reactivity, expanding the application potential of bio-tar-derived carbons in areas such as high-performance supercapacitor electrodes, gas adsorption, or catalytic supports.

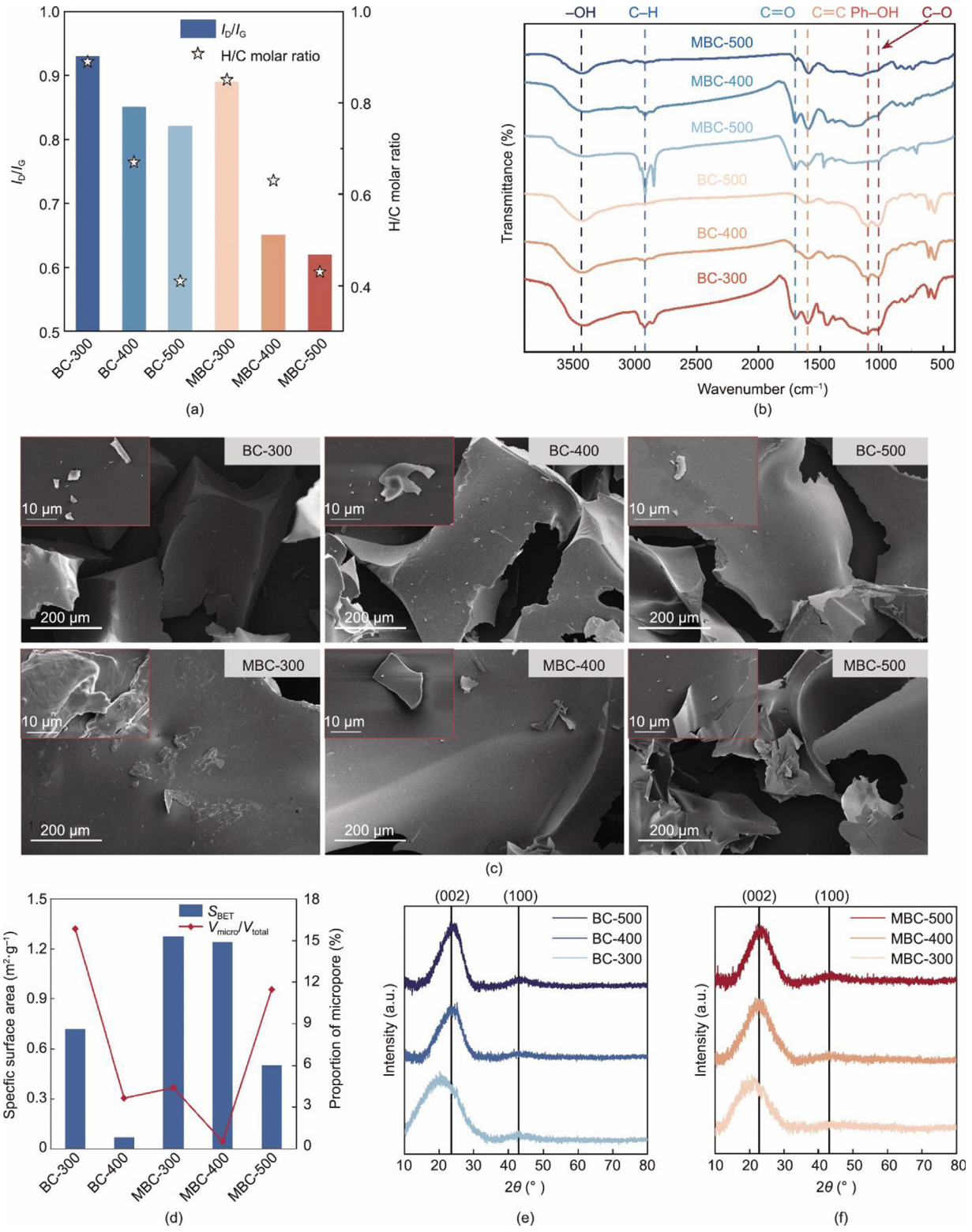

Fig. 4. Physicochemical characterization of the polymerization products. (a) Graphitization degree. (b) FTIR spectra. (c) SEM images. (d) Porosity characteristics. Comparative XRD patterns of the (e) bio-tar polymerization products (BC-*x*) and (f) M-bio-tar polymerization products (MBC-*x*). 2θ: diffraction angle. BC-300, BC-400, and BC-500 denote the bio-carbons derived from bio-tar polymerized at 300, 400, and 500 °C, respectively. Similarly, MBC-300, MBC-400, and MBC-500 represent the bio-carbons derived from model bio-tar under the same respective polymerization temperatures.

3.5. Thermodynamic feasibility and experimental validation

DFT calculations were systematically conducted to evaluate the thermodynamic feasibility of the polymerization pathways and the molecular orbital interactions governing bio-tar carbonization [56]. The HOMO–LUMO energy gap (ΔE) of the model compounds provides important insights into their tendency to undergo polymerization (Table S7 in Appendix A). The relatively small ΔE of

phenol (6.06 eV) indicates its high reactivity, effectively facilitating the electron transfer necessary to initiate, radical-driven crosslinking. Meanwhile, the moderately narrow energy gaps of furan (ΔE = 6.59 eV) and benzyl alcohol (ΔE = 6.54 eV) support their dual function as volatile byproducts and contributors to the polymerization process, consistent with experimental data. In contrast, the broader energy gaps of compounds enriched with oxygen, such as benzoic acid (ΔE = 5.65 eV) and methyl benzoate (ΔE = 5.67 eV), stemming from their electron-withdrawing carboxyl and ester groups, render them more prone to decarboxylation and subsequent CO_2 release during thermal treatment. Notably, glucose (ΔE = 5.61 eV) and benzaldehyde (ΔE = 5.09 eV) exhibited exceptionally low LUMO energies (–1.90 to –1.40 eV), promoting nucleophilic attacks on electron-rich aromatic systems to drive the C=C bond and furanic intermediate formation for Diels–Alder reactions. Hydrocarbons such as paraffin (ΔE = 10.05 eV) and toluene (ΔE = 6.60 eV) showed significant variations in their energy gap, explaining the temperature-enhanced hydrocarbon volatilization and the limited contribution of small aromatics to carbon precursor formation [57].

Gibbs free energy change (ΔG) calculations for key polymerization reactions (Table 1) revealed temperature-driven thermody-

Table 1
Gibbs free energy change (ΔG) calculations for key polymerization reactions.

No.	Reaction equation	ΔG at 0 K (kcal·mol^{-1})	ΔG at 573.15 K (kcal·mol^{-1})
1	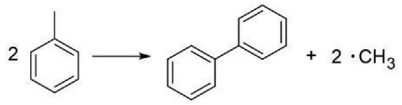	76.2	69.45
2	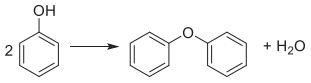	3.47	7.96
3	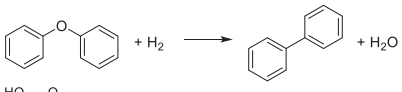	–21.88	–24.29
4	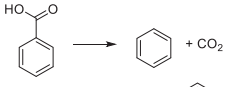	–15.17	–22.82
5	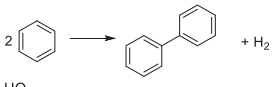	7.25	7.64
6	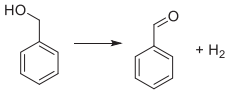	1.42	–7.05
7	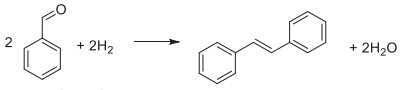	–18.35	–7.75
8	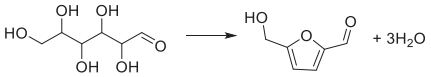	–47229.86	–47263.92
9	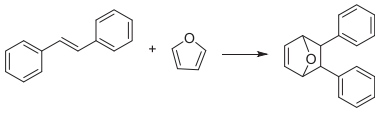	16.81	30.09
10	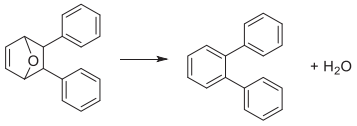	–48.93	–60.34
11	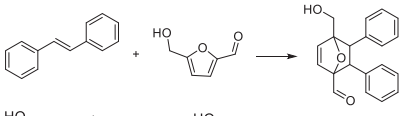	21.63	37.03
12	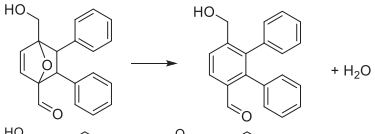	–50.77	–62.67
13	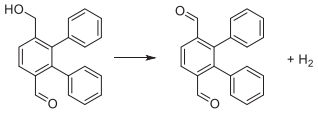	3.59	–3.81
14	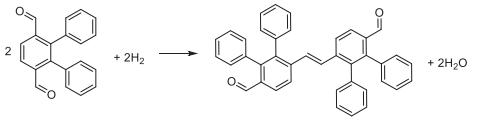	–22.75	–11.25

namic preferences (Fig. 5). Phenol-toluene systems predominantly form multiphenyl structures through C–C-ether linkages via $R^{\bullet}$, $HO^{\bullet}$, and $H^{\bullet}$ elimination, ultimately generating biphenyl-like precursors via dehydrogenation [58]. Carboxylic acids (e.g., benzoic acid) undergo decarboxylation to produce aromatic hydrocarbons (e.g., benzene), which aligns with the HOMO-LUMO predictions. In addition to radical-driven pathways, oxygen-functionalized crosslinking emerged as a major route. Elevated temperatures intensify the electron-deficient character of alcohols, promoting their oxidation to aldehydes. These aldehydes undergo dehydration-driven polymerization to form C=C bonds, thereby increasing the molecular carbon content. Moreover, the aldehydes reacted with furanic intermediates originating from sugar decomposition, such as furan and 5-hydroxymethylfurfural, to generate oxygen-bridged structures. Subsequent cleavage of these bridges, along with deoxygenation, leads to the formation of polycyclic aromatic precursors containing three or more rings. Notably, sugar-derived furans bearing hydroxyl groups act synergistically with the thermally facilitated conversion of alcohols to aldehydes, further accelerating the polymerization process [59].

To specifically probe the key roles of the furan ring and aldehyde group, three sets of validation experiments were conducted: adding furan or benzaldehyde separately, and adding both compounds simultaneously at levels matching their relative contents in the M-bio-tar. Polymerization was performed at 300 °C, with other conditions consistent with bio-carbon preparation (Table S8 in Appendix A). Increasing the relative content of the furan ring and the aldehyde group substantially enhanced the

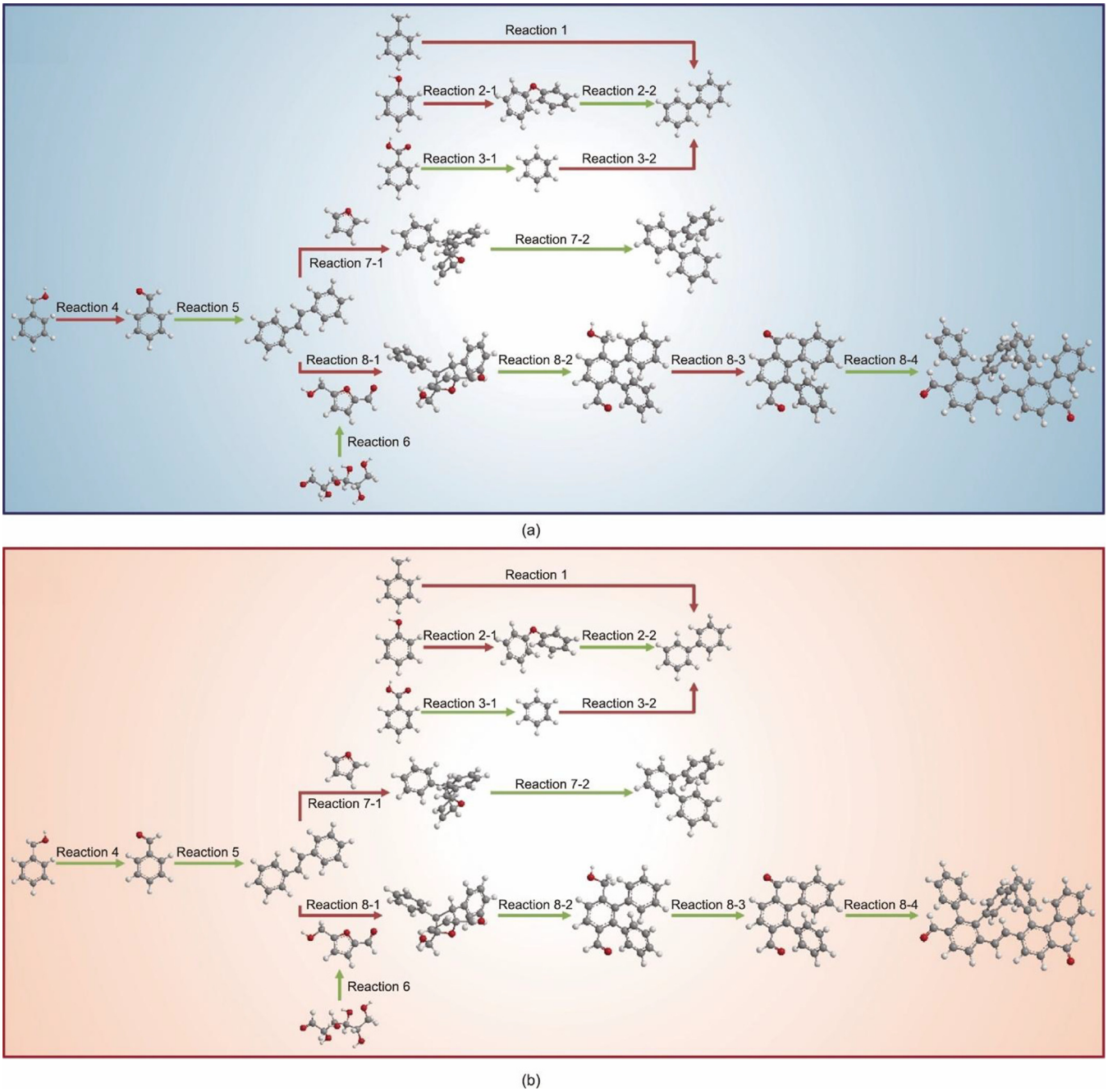

Fig. 5. Gibbs-free-energy-driven polymerization pathways and carbon precursor formation in M-bio-tar (green/red arrows: $\Delta G < 0/\Delta G > 0$). (a) Computational modeling at 0 K. (b) Computational modeling at 573.15 K.

bio-carbon yield by 12.21% and 35.40%, respectively. This confirms the promoting effect of these oxygen-containing functional groups on bio-tar polymerization, consistent with the DFT calculations. The stronger effect observed for benzaldehyde can be attributed to its additional benzene ring, which facilitates the formation of carbon precursors. Notably, concurrently increasing the relative contents of the aldehyde group and the furan ring while maintaining their ratio led to an even more pronounced increase of 51.15% in the polymerization efficiency. This synergistic effect, which exceeds the sum of the individual enhancements, indicates cooperative interactions between the functional groups. These findings further support the mechanistic insight that aldehyde conversion supplies key intermediates for furan-involved polymerization reactions.

This computational framework, along with the experimental validation, correlates molecular thermodynamics with macroscopic bio-tar composition. Oxygen functionalities, particularly aldehydes and furans, are critical for spontaneous polymerization. Although hydrocarbons participate in crosslinking via radical-mediated bond cleavage and cyclization, their volatility (aromatics) or stability (aliphatics) limits their contributions. Thus, enriching oxygenated groups (especially aldehydes and furans) via component modulation or pretreatment can be envisaged as a key strategy to increase bio-carbon yield, consistent with prior studies. These insights establish principles for optimizing bio-tar immobilization efficiency. However, the inherent temperature hysteresis between volatile release and carbon skeleton formation limits the improvement of porosity via compositional tuning. Future research should focus on the directional modulation of the content and types of key reactive functional groups in bio-tar through feedstock pretreatment to enhance polymerization efficiency and optimize the initial pore structure of the carbon material. Post-synthesis modifications are recommended to increase the application potential of bio-carbon, particularly for porous materials. These strategies will help advance the practical application of bio-tar-derived carbon materials in fields such as energy storage, environmental remediation, and green catalysis, enabling the deep integration of waste valorization and high-value utilization.

4. Conclusions

This study systematically deciphers the mechanistic framework governing bio-tar thermal polymerization and its transformation into functional carbon materials. By integrating the M-bio-tar system, multistage thermokinetic analyses, and computational simulations, a temperature-mediated stage-specific polymerization mechanism: volatile evaporation ($\leq$ 200 °C), radical-mediated intermediate crosslinking (200–400 °C), and carbon skeleton consolidation ($\geq$ 300 °C) is revealed. The M-bio-tar, designed to reflect the compositional heterogeneity of native bio-tar, successfully replicates key thermal behaviors while enabling the isolation of functional group-specific contributions. Radical dynamics involving $R^{\bullet}$ and $HO^{\bullet}$ are key contributors to crosslinking processes, while oxygenated intermediates such as aldehydes and furans enhance polymerization efficiency via synergistic Diels–Alder and cyclization reactions. Structural evolution analyses reveal temperature-dependent trade-offs among graphitization, dehydrogenation, and porosity development. This work bridges the gap between waste management and functional material design, advancing the rational development of biomass-derived carbon materials and contributing to the circular bioeconomy while aligning with global sustainability goals in energy and environmental technologies.

CRediT authorship contribution statement

Yuxuan Sun: Writing – original draft, Methodology, Investigation, Formal analysis. **Lixin Zhao:** Writing – review & editing, Supervision, Conceptualization. **Huiyan Zhang:** Writing – review & editing, Supervision. **Hui Zhou:** Writing – review & editing, Supervision, Resources. **Lili Huo:** Writing – review & editing, Supervision, Conceptualization. **Jixiu Jia:** Writing – review & editing, Resources. **Zonglu Yao:** Writing – review & editing, Supervision, Resources, Project administration, Methodology.

Declaration of competing interest

The authors declare that they have no known competing financial interests or personal relationships that could have appeared to influence the work reported in this paper.

Acknowledgments

This work was supported by the National Natural Science Foundation of China (52376220) and the Central Public-interest Scientific Institution Basal Research Fund (Y2025YC32).

Appendix A. Supplementary data

Supplementary data to this article can be found online at https://doi.org/10.1016/j.eng.2026.02.034.

References

[1] Xu X, Zhang X, Zou Y, Chen T, Zhan J, Cheng L, et al. Integrated carbon and nitrogen management for cost-effective environmental policies in China. Science 2025;388(6751):1098–103.
[2] Li T, Chen C, Brozena AH, Zhu JY, Xu L, Driemeier C, et al. Developing fibrillated cellulose as a sustainable technological material. Nature 2021;590(7844):47–56.
[3] Yao Z, Kang K, Cong H, Jia J, Huo L, Deng Y, et al. Demonstration and multi-perspective analysis of industrial-scale co-pyrolysis of biomass, waste agricultural film, and bituminous coal. J Clean Prod 2021;290:125819.
[4] Hong L, Zhang H, Hu L, Xiao R, Chu S. Near-infrared light-driven biomass conversion. Sci Adv 2024;10(30):eadn9441.
[5] Luo Z, Liu C, Radu A, de Waard DF, Wang Y, Behaghel De Bueren JT, et al. Carbon–carbon bond cleavage for a lignin refinery. Nat Chem Eng 2024;1(1):61–72.
[6] Al-Rumaihi A, Shahbaz M, Mckay G, Mackey H, Al-Ansari T. A review of pyrolysis technologies and feedstock: a blending approach for plastic and biomass towards optimum biochar yield. Renew Sustain Energy Rev 2022;167:112715.
[7] Shen D, Jin W, Hu J, Xiao R, Luo K. An overview on fast pyrolysis of the main constituents in lignocellulosic biomass to valued-added chemicals: structures, pathways and interactions. Renew Sustain Energy Rev 2015;51:761–74.
[8] McLaughlin H, Littlefield AA, Menefee M, Kinzer A, Hull T, Sovacool BK, et al. Carbon capture utilization and storage in review: sociotechnical implications for a carbon reliant world. Renew Sustain Energy Rev 2023;177:113215.
[9] Jia J, Sun Y, Liu Z, Liu Z, Huo L, Kang K, et al. Waste bio-tar based N-doped porous carbon for supercapacitors under dual activation: performance, mechanism, and assessment. Biochar 2023;5(1):91.
[10] Jia J, Sun Y, Huo L, Zhao L, Liu Z, Liu Z, et al. Bio-carbon composite for supercapacitor electrodes: harnessing hydrochar frameworks and bio-tar polymerization. Fuel Process Technol 2025;269:108178.
[11] Cheng BH, Huang BC, Zhang R, Chen YL, Jiang SF, Lu Y, et al. Bio-coal: a renewable and massively producible fuel from lignocellulosic biomass. Sci Adv 2020;6(1):eaay0748.
[12] Sun Y, Jia J, Huo L, Zhang X, Zhao L, Liu Z, et al. Preparation of bio-carbon by polymerization of bio-tar: a critical review on mechanisms, processes, and applications. Biochar 2025;7(1):90.
[13] Mohanty AK, Vivekanandhan S, Das O, Romero Millán LM, Klinghoffer NB, Nzihou A, et al. Biocarbon materials. Nat Rev Methods Primers 2024;4(1):19.
[14] Sun Y, Sun P, Jia J, Liu Z, Huo L, Zhao L, et al. Machine learning in clarifying complex relationships: biochar preparation procedures and capacitance characteristics. Chem Eng J 2024;485:149975.
[15] Sun Y, Jia J, Liu Z, Liu Z, Huo L, Zhao L, et al. Heteroatom-doped biochar devised from cellulose for CO_2 adsorption: a new vision on competitive behavior and interactions of n and s. Biochar 2023;5(1):76.
[16] Font PC. Modelling of tar formation and evolution for biomass gasification: a review. Appl Energy 2013;111:129–41.

[17] Shukla B, Koshi M. Comparative study on the growth mechanisms of PAHs. Combust Flame 2011;158(2):369–75.
[18] Hu X, Nango K, Bao L, Li T, Hasan MDM, Li C. High yields of solid carbonaceous materials from biomass. Green Chem 2019;21(5):1128–40.
[19] Cao M, Reaihan E, Yuan C, Rosendahl LA, Zhang Y, Xu CC, et al. Green coal and lubricant via hydrogen-free hydrothermal liquefaction of biomass. Nat Commun 2025;16(1):722.
[20] Chu C, Ma LL, Alawi H, Ma W, Zhu Y, Sun J, et al. Mechanistic exploration of polytetrafluoroethylene thermal plasma gasification through multiscale simulation coupled with experimental validation. Nat Commun 2024;15(1):1654.
[21] Luo N, Montini T, Zhang J, Fornasiero P, Fonda E, Hou T, et al. Visible-light-driven coproduction of diesel precursors and hydrogen from lignocellulose-derived methylfurans. Nat Energy 2019;4(7):575–84.
[22] Hsu K, Li S, Micari M, Chi H, Villalobos LF, Huang S, et al. Graphene membranes with pyridinic nitrogen at pore edges for high-performance CO_2 capture. Nat Energy 2024;9(8):964–74.
[23] Xiong Z, Wang Y, Syed-Hassan SSA, Hu X, Han H, Su S, et al. Effects of heating rate on the evolution of bio-oil during its pyrolysis. Energy Convers Manage 2018;163:420–7.
[24] Xuan W, Gao J, Ma Z, Cao C, Yan S, Wang Q. Synergistic mechanism and radicals interaction of the co-pyrolysis of lignite and pe based on reaxff-md and dft. Energy 2024;289:129978.
[25] Xie T, Zhao L, Yao Z, Kang K, Jia J, Hu T, et al. Co-pyrolysis of biomass and polyethylene: insights into characteristics, kinetic and evolution paths of the reaction process. Sci Total Environ 2023;897:165443.
[26] Zhou YJ, Kerkhoven EJ, Nielsen J. Barriers and opportunities in bio-based production of hydrocarbons. Nat Energy 2018;3(11):925–35.
[27] Lei J, Zhang Y, Yao Y, Shi Y, Leung KL, Fan J, et al. An active and durable molecular catalyst for aqueous polysulfide-based redox flow batteries. Nat Energy 2023;8(12):1355–64.
[28] Pan Y, Zhang H, Zhang B, Gong F, Feng J, Huang H, et al. Renewable formate from sunlight, biomass and carbon dioxide in a photoelectrochemical cell. Nat Commun 2023;14(1):1013.
[29] Wang T, Pan R, Martins ML, Cui J, Huang Z, Thapaliya BP, et al. Machine-learning-assisted material discovery of oxygen-rich highly porous carbon active materials for aqueous supercapacitors. Nat Commun 2023;14(1):4607.
[30] Salanne M, Rotenberg B, Naoi K, Kaneko K, Taberna PL, Grey CP, et al. Efficient storage mechanisms for building better supercapacitors. Nat Energy 2016;1(6):16070.
[31] Xu Z, Mapstone G, Coady Z, Wang M, Spreng TL, Liu X, et al. Enhancing electrochemical carbon dioxide capture with supercapacitors. Nat Commun 2024;15(1):7851.
[32] Zhu X, Lin L, Pang M, Jia C, Xia L, Shi G, et al. Continuous and low-carbon production of biomass flash graphene. Nat Commun 2024;15(1):3218.
[33] Li N, Yan K, Rukkijakan T, Liang J, Liu Y, Wang Z, et al. Selective lignin arylation for biomass fractionation and benign bisphenols. Nature 2024;630(8016):381–6.
[34] Vinu R, Broadbelt LJ. A mechanistic model of fast pyrolysis of glucose-based carbohydrates to predict bio-oil composition. Energy Environ Sci 2012;5(12):9808–26.
[35] Xiong Z, Chen Y, Azis MM, Hu X, Deng W, Han H, et al. Roles of furfural during the thermal treatment of bio-oil at low temperatures. J Energy Chem 2020;50:85–95.
[36] Qiu B, Liu M, Qu X, Zhou F, Xie H, Wang D, et al. Waste plastics upcycled for high-efficiency H_2O_2 production and lithium recovery via Ni-Co/carbon nanotubes composites. Nat Commun 2024;15(1):6473.
[37] Zhang Y, Peng G, Li S, Wu H, Chen K, Wang J, et al. Phase interface engineering enables state-of-the-art half-Heusler thermoelectrics. Nat Commun 2024;15(1):5978.
[38] Yu S, Dong X, Zhao P, Luo Z, Sun Z, Yang X, et al. Decoupled temperature and pressure hydrothermal synthesis of carbon sub-micron spheres from cellulose. Nat Commun 2022;13(1):3616.
[39] Xie T, Huo L, Yao Z, Zhang X, Liu Z, Jia J, et al. Co-pyrolysis of biomass and polyethylene: mechanistic insights into functional group transformations on solid matrix. Chem Eng J 2024;482:149166.
[40] Rubin EM. Genomics of cellulosic biofuels. Nature 2008;454(7206):841–5.
[41] Zhang X, Huo L, Yao Z, Xie T, Jia J, Sun Y, et al. Pyrolysis characteristics and hydrogen production mechanism of biomass impregnated with transition metals. J Clean Prod 2024;474:143572.
[42] Huang X, Yin H, Zhang H, Mei N, Mu L. Pyrolysis characteristics, gas products, volatiles, and thermo-kinetics of industrial lignin via TG/DTG-FTIR/MS and in-situ Py-PI-TOF/MS. Energy 2022;259:125062.
[43] Wu L, Guan Y, Li C, Shi L, Yang S, Rajasekhar Reddy B, et al. Free-radical behaviors of co-pyrolysis of low-rank coal and different solid hydrogen-rich donors: a critical review. Chem Eng J 2023;474:145900.
[44] Wu Y, Zhu J, Yang J, Jin L, Hu H. Insight into co-pyrolysis interaction of Pingshuo coal and low-density polyethylene under varied mixing configurations via *in-situ* Py-TOF-MS. J Anal Appl Pyrolysis 2022;168:105698.
[45] Zhu Y, Chen M, Li Q, Yuan C, Wang C. High-yield humic acid-based hard carbons as promising anode materials for sodium-ion batteries. Carbon 2017;123:727–34.
[46] Chen P, Yang R, Pei Y, Yang Y, Cheng J, He D, et al. Hydrothermal synthesis of similar mineral-sourced humic acid from food waste and the role of protein. Sci Total Environ 2022;828:154440.
[47] Shutthanandan V, Nandasiri M, Zheng J, Engelhard MH, Xu W, Thevuthasan S, et al. Applications of XPS in the characterization of battery materials. J Electron Spectrosc Relat Phenom 2019;231:2–10.
[48] Guo X, Fang G, Li G, Ma H, Fan H, Yu L, et al. Direct, nonoxidative conversion of methane to ethylene, aromatics, and hydrogen. Science 2014;344(6184):616–9.
[49] Wu Y, Zhao Y, Yuan Q, Sun H, Wang A, Sun K, et al. Electrochemically synthesized H_2O_2 at industrial-level current densities enabled by in situ fabricated few-layer boron nanosheets. Nat Commun 2024;15(1):10843.
[50] Zhu Y, Cao Y, Fu B, Wang C, Shu S, Zhu P, et al. Waste milk humification product can be used as a slow release nano-fertilizer. Nat Commun 2024;15(1):128.
[51] Yang F, Zhang S, Cheng K, Antonietti M. A hydrothermal process to turn waste biomass into artificial fulvic and humic acids for soil remediation. Sci Total Environ 2019;686:1140–51.
[52] Zhang J, Lü F, Luo C, Shao L, He P. Humification characterization of biochar and its potential as a composting amendment. J Environ Sci (China) 2014;26(2):390–7.
[53] Ait Baddi G, Hafidi M, Cegarra J, Alburquerque JA, Gonzálvez J, Gilard V, et al. Characterization of fulvic acids by elemental and spectroscopic (FTIR and ^{13}C-NMR) analyses during composting of olive mill wastes plus straw. Bioresour Technol 2004;93(3):285–90.
[54] Huang P, Zhang P, Wang C, Tang J, Sun H. Enhancement of persulfate activation by Fe-biochar composites: synergism of Fe and N-doped biochar. Appl Catal B 2022;303:120926.
[55] Wohlgemuth S, Vilela F, Titirici M, Antonietti M. A one-pot hydrothermal synthesis of tunable dual heteroatom-doped carbon microspheres. Green Chem 2012;14(3):741–9.
[56] Yuan D, Zhang C, Tang S, Li X, Tang J, Rao Y, et al. Enhancing CaO_2 fenton-like process by Fe(II)-oxalic acid complexation for organic wastewater treatment. Water Res 2019;163:114861.
[57] Zhu X, Deng W, Chiou MF, Ye C, Jian W, Zeng Y, et al. Copper-catalyzed radical 1,4-difunctionalization of 1,3-enynes with alkyl diacyl peroxides and N-Fluorobenzenesulfonimide. J Am Chem Soc 2019;141(1):548–59.
[58] Chen K, Li J, Zhang Y, Chen B. The impact of different functional groups of biochar on mercury adsorption investigated by density functional theory. J Clean Prod 2025;486:144546.
[59] Wei Z, Li Y, Wang Y, He Z. Mechanism investigations on co-pyrolysis of polyethylene and biomass using ReaxFF simulation and DFT computation. J Environ Chem Eng 2023;11(5):110808.